A first-principles reassessment of the Fe-N phase diagram in the low-nitrogen limit

Sam De Waele[a,b,*], Kurt Lejaeghere[a], Elke Leunis[c], Lode Duprez[c], Stefaan Cottenier[a,b,**]

[a] *Center for Molecular Modeling, Ghent University. Technologiepark 903, 9052 Zwijnaarde, Belgium*
[b] *Department of Electrical Energy, Metals, Mechanical Constructions and Systems, Ghent University. Technologiepark 913, 9052 Zwijnaarde, Belgium*
[c] *OCAS NV. Technologiepark 935, 9052 Zwijnaarde, Belgium*

Abstract

Nitriding of steels has been widely used for almost a century. However, insight in two important precipitating phases for low concentration through-thickness nitriding is still lacking, hindering further development of the process. Due to their metastable nature, manufacturing large homogeneous samples of Fe_4N and $Fe_{16}N_2$ is very challenging. Consequently, measuring thermodynamic properties, such as heat capacity and free energy, has proven difficult at best. In this work, we have calculated those thermodynamic properties using density-functional theory (DFT) for Fe_4N, $Fe_{16}N_2$ and ferrite with nitrogen in solid solution. This information is a necessary prerequisite to improve the accuracy of larger-scale modeling approaches of iron nitrides. We used the free energies to construct the temperature/concentration phase diagram for low nitrogen concentrations from 0 K to 865 K. Both the range of metastability for $Fe_{16}N_2$ and the nitrogen solvus confirm the experimental data. On the other hand, it was concluded that the experimental Curie temperature for $Fe_{16}N_2$ is severely underestimated because of the thermodynamic instability above 400 K.

Keywords: Nitride materials Thermodynamic properties Precipitation Magnetization Computer Simulations Density-functional theory

1. Introduction

Nitrogen is present in all steels as a residual element. In some cases, nitrogen is even added intentionally as an alloying element. Nitriding is a gaseous thermochemical treatment that is widely used to improve the surface properties of parts and components made in forging and tool steel.[1, 2, 3, 4] Indeed, during nitriding, a compound layer at the surface and a diffusion zone underneath are

*Corresponding author. E-mail address: sdwaele.dewaele@ugent.be
**Principal corresponding author. E-mail address: stefaan.cottenier@ugent.be

formed. In contrast, through-thickness nitriding for improvement of bulk properties is rarely considered. By selecting the appropriate nitriding conditions, the formation of a compound layer at the surface can be avoided and, for pure $\alpha-$Fe or for ferritic steels with no nitride forming elements present, the absorbed nitrogen will be in solid solution during nitriding. If the cooling is fast enough, the nitrogen will stay in solid solution up to room temperature, resulting in a solid solution strengthening of 50 MPa per 0.01 wt% of added nitrogen.[5] For low nitrogen concentrations, slow cooling can produce the bulk precipitation of Fe_4N or $Fe_{16}N_2$.[6]

The knowledge of the thermodynamic stability and nucleation rate of precipitates or phases is essential to fully understand the thermal and mechanical properties of the manufactured steel. With respect to these aspects, the Fe-C system is relatively well studied, but such information is not generally available for the Fe-N system, due to the metastability of the Fe-N phases or the unavailability of the phases in pure form.[7] Because experimental data on phase equilibria in the Fe-N system are often limited to narrow temperature ranges, a computational approach offers a complementary alternative.

Thermodynamic properties such as the heat capacity and the thermal expansion are essential to describe the iron nitrides in large-scale approaches, such as phase field models,[8] but they require the knowledge of free energies for each phase. Previous derivations of the free energy for Fe_4N were based on solvus lines in the phase diagram[9] or the cluster variation method (CVM) combined with the Debye-Grüneisen model.[10] In contrast to such (semi-)empirical, using density-functional theory (DFT) provides a non-empirical approach for modeling the iron nitrides.[11, 12] This avoids the process of extrapolating phase stability from narrow temperature ranges and provides insight into the relative stability of Fe with N in solid solution ($Fe_{[N]}$), Fe_4N and $Fe_{16}N_2$ from 1000 K down to 0 K. On the other hand, the complexity and size of crystal structures that are feasible to tackle with DFT calculations are limited. Consequently, this work is restricted to the line compounds Fe_4N and Fe_16N_2 and does not take into account the disorder associated with possible off stoichiometries that are experimentally observed.[13, 14] To capture said off-stoichiometric disorder, a dedicated approach, such as the Gorsky-Bragg-Williams method,[?] as employed by Kooi *et al.*,[15] the cluster variation method used by Pekelharing *et al.*,[16][17] the use of semi quasi random structures[18] or the cluster expansion model[19] would be necessary.

To obtain the free energies for Fe and iron nitrides, all relevant contributions should be taken into account: electronic, vibrational, magnetic and configurational. The electronic free energy is obtained using finite-electron temperature DFT,[20] the quasiharmonic approximation is used to compute the vibrational free energy and a rescaled Monte Carlo approach is applied for the magnetic excitations.[21, 22] The free energies can subsequently be used to evaluate the phase equilibria between the various phases, yielding the tempera-

ture/composition phase diagram of Fe_4N, $Fe_{16}N_2$ and bcc $Fe_{[N]}$ for N concentrations below 1 at.%.

2. Methodology

The free energy is determined for bcc iron (Fe), iron with N in solid solution ($Fe_{[N]}$), Fe_4N and $Fe_{16}N_2$. The iron nitride $Fe_{16}N_2$ is ferromagnetically ordered and has the space group $I4/mmm$.[23] The nitrogen atoms occupy the regular octahedral interstitial positions $(0.0, 0.0, 0.0)$ and $(0.5, 0.5, 0.5)$ in a distorted bcc iron lattice [Fig. 1a], which is the 1b Wyckoff position. This regular ordering of the nitrogen atoms causes a macroscopic tetragonal distortion. Fe_4N is a ferromagnetic material as well, but in contrast to $Fe_{16}N_2$ it has a cubic crystallography with space group $P\,m\,\overline{3}\,m$.[24] The iron atoms form a face-centered cubic sublattice, with the nitrogen atom occupying the $(0.5, 0.5, 0.5)$ 1b Wyckoff position [Fig. 1b].

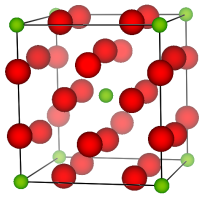

(a) The crystallographic unit cell of $Fe_{16}N_2$.

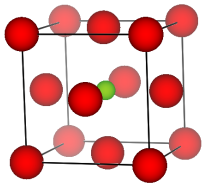

(b) The crystallographic unit cell of Fe_4N.

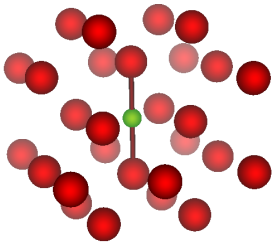

(c) A nitrogen impurity in a bcc iron lattice. It occupies an octahedral interstitial position. The two nearest iron neighbors and the nitrogen atom are aligned, which causes a local tetragonal distortion.

Figure 1: Crystallography of the three considered Fe-N phases with the Fe atoms shown in red and the N atoms in green.

To completely describe the equilibria between these phases, the defect free en-

ergy of nitrogen in solid solution is needed as well. As an impurity in body-centered iron, nitrogen forms an interstitial defect in an octahedral configuration [Fig. 1c].[25] In this position, the nitrogen impurity aligns with its nearest iron neighbors. This causes a local tetragonal distortion, where especially the aligned iron atoms undergo a large displacement from their original bcc position. For every Fe host atom, there are 3 interstitial octahedral sites.

To determine the volume-and temperature-dependent Helmholtz free energy F for every phase, the electronic, vibrational and magnetic excitations are determined. For bcc Fe with N in solid solution, the configurational contribution as a function of the N concentration c must be taken into account as well. The common assumption is that these contributions are all adiabatically decoupled, *i.e.* $F(V,T,c)$ can be written as:[26]

$$\begin{aligned} F(V,T,c) =& F_{el}(V,T) + F_{vib}(V,T) \\ &+ F_{mag}(V,T) + F_{conf}(T,c), \end{aligned} \tag{1}$$

where F_{el}, F_{vib}, F_{mag} and F_{conf} are the electronic, vibrational, magnetic and configurational contributions, respectively. For the $Fe_{[N]}/Fe_4N$ and $Fe_{[N]}/Fe_{16}N_2$ phase equilibria, the nitrogen concentrations in iron are below 1 at.%.[27] Consequently, F_{conf} can be calculated from the configurational entropy for a dilute solution:[28]

$$F_{conf}(T,c) = -Tk_b \left[c - c\ln(c) + c\ln(g)\right], \tag{2}$$

where k_b is the Boltzman constant, c is the nitrogen concentration and $g = 3$ the number of interstitial sites per host atom. Including all contributions eventually allows the derivation of the equilibrium volume $V_0(T)$at a given pressure P and temperature T:

$$\frac{\partial F(V,T)}{\partial V} = -P, \tag{3}$$

which ultimately yields the free energy under (P,T) conditions.

2.1. Electronic Free Energy

The electronic contribution $F_{el}(V,T)$ is obtained from a set of DFT calculations at different volumes and electron temperatures.[20] After an initial optimization of the atomic positions and volume, the total energy is calculated for volumes ranging from 94 % to 106 % of the initial equilibrium volume and for electron temperatures between 2 K to 1000 K. Following the approach proposed by Grabowski *et al.*,[29] the electronic free energy is separated into two contributions:

$$F_{el}(V,T) = E_0(V) + \widetilde{F}_{el}(V,T). \tag{4}$$

The different contributions to $F_{el}(V,T)$ are subsequently parametrized into an analytical form, which facilitates the derivation of entropy and heat capacity. The energies for the different volumes at the lowest temperature ($T = 2\,\mathrm{K}$) are used to fit the 0 K volume-dependent behavior $E_0(V)$ to a Birch-Murnaghan equation of state.[30] This determines the equilibrium volume, internal energy, bulk modulus and the derivative of the bulk modulus with respect to the pressure. For the temperature dependence one uses

$$\begin{aligned}\widetilde{F}_{el}(V,T) = \frac{1}{2}Tk_b \left\{\sum_{i=1}^{3}(\alpha_i + V\beta_i)T^i\right\} \\ \times \int d\epsilon \big[f(T,\epsilon)\ln f(T,\epsilon) \\ + (1-f(T,\epsilon))\ln(1-f(T,\epsilon))\big],\end{aligned} \tag{5}$$

which is based on the general electronic entropy [31]

$$\widetilde{F}_{el}(V,T) \approx -\frac{1}{2}TS_{el}(V,T) \tag{6}$$

and

$$\begin{aligned}S_{el}(V,T) = -k_b \int d\epsilon\ N_{el}(V,T,\epsilon)[f(T,\epsilon)\ln f(T,\epsilon) \\ + (1-f(T,\epsilon))\ln(1-f(T,\epsilon))]\end{aligned} \tag{7}$$

The function f is the level occupation described by the Fermi-Dirac distribution. The electronic density of states N_{el} is replaced by the energy-independent average

$$N_{el}(V,T) = \sum_{i=1}^{3}(\alpha_i + V\beta_i)T^i. \tag{8}$$

Here, α_i and β_i are six fitting parameters that fully describe the temperature-dependent part of F_{el} and the temperature-induced volume dependence. The linear parametrization in volume combined with the third-order polynomial parametrization in temperature produces a maximum residual error of well below 0.1 meV/atom.

All calculations of F_{el} were performed with the Vienna Ab Initio Simulation Package (VASP), [31, 32] using VASP 5.4 recommended PAW potentials.[33, 34] For the Fe atoms, the PAW potential with 8 valence electrons was used ([Ar] $3d^6\ 4s^2$), while for N the potential with 5 valence electrons was used ([He] $2p^3\ 2s^2$). These potentials were recently shown to provide a similar precision as all-electron calculations. [35] The Perdew-Burke-Ernzerhof (PBE) exchange-correlation functional was used in most cases,[36] but the local density approximation (LDA) as parametrized by Perdew and Zunger[37] was, where useful,

evaluated as well. The Brillouin zone integration grid always contained at least $27\,648/N_{atoms}$ $\vec{k}$-points, with N_{atoms} the number of atoms in the unit cell. Fermi smearing, with the smearing parameter σ determined by the required temperature, was used for the electronic self-consistent field cycle with a convergence criterion of 10^{-9} eV. A conjugate-gradient algorithm was used for the geometric optimization with a convergence criterion of 10^{-8} eV. An energy cutoff of 500 eV was used for the plane wave basis sets, with the grid for fast Fourier transform able to capture reciprocal vectors twice as large as the vectors included in the basis set. The input files for all the calculations used in this work can be found in the supplementary information.

2.2. Vibrational free energy of $Fe_{[N]}$, Fe_4N and $Fe_{16}N_2$

The lattice vibrations are included using the quasiharmonic approximation. To account for thermal expansion, phonon spectra are computed for volumes relevant to the thermal expansion; *i.e.* ranging from 99 % to 106 % of the equilibrium volume. The volume-dependent frequencies $\omega_i(V)$ thus obtained are used to calculate the vibrational free energy:[26]

$$F_{vib}(V,T) = \frac{1}{3N}\sum_{i=1}^{3N}\left\{\frac{1}{2}\hbar\omega_i(V) + k_BT\ln\left[1-\mathrm{e}^{-\hbar\omega_i(V)/k_BT}\right]\right\}. \tag{9}$$

Here, N is the number of sampled points in reciprocal space multiplied by the number of atoms in the unit cell.

The phonon spectra were constructed using the direct force constant method.[38] Various supercells with atomic displacements of 0.01 Å were set up using the phonopy software package.[39] The forces in response to the displacements were calculated with DFT using VASP. Compared to the calculations of F_{el} an additional support grid was used for the augmentation charges. Moreover, instead of Fermi smearing, first-order Methfessel-Paxton smearing with $\sigma = 0.2$ eV was used for electronic convergence.[40] The simulated supercells were made large enough so that the minimum distance between periodic images was at least 11 Å. The diagonalization of the dynamical matrix was performed with the phonopy software again, after which each frequency from the different phonon spectra was fitted to a quadratic function of volume. This use of a second-order polynomial is sufficient to limit the maximum residual error to 0.01 THz for all frequencies. Even for the smallest frequencies, this results in an error below 1 % for the vibrational free energy.

2.3. Magnetic contribution

Directly calculating magnetic free energies with DFT is not yet possible. Instead, utilizing an atom-centered model has proven to be a successful approximation for iron and its alloys. More specifically, the Heisenberg model will be used as magnetic Hamiltonian:[41, 42, 43, 44, 45, 46, 47, 22]

$$H = -\frac{1}{2}\sum_{i \neq j} J_{ij}\ \vec{M}_i \cdot \vec{M}_j \tag{10}$$

The sum in Eq. 10 is taken for all atom pairs in the solid, with M_i the local magnetic moments and J_{ij} the Heisenberg exchange coupling parameters. The former are easily obtained from DFT calculations, but the latter require a somewhat more involved derivation. There are multiple ways of obtaining the coupling parameters. In this work, a DFT calculation based on the Korringa-Kohn-Rostoker Green's function method[48, 49] was performed using the SPR-KKR software.[50, 51] This allows direct access to the J_{ij} using the formulation of Liechtenstein *et al.*[52]

To determine $F_{mag}(T)$ from Eq. 10, classical Metropolis Monte Carlo (cMC) calculations were performed with the ALPS software.[53, 54, 55] To do this, the sum in equation 10 is truncated at a threshold for the J_{ij}. This truncation was determined by evaluating the mean-field Curie temperature as a function of the threshold value. The mean-field Curie temperature is equal to the largest eigenvalue of the coupling parameters matrix $\mathbf{J}$ with[56]

$$\mathbf{J}_{\alpha,\beta} = \sum_{\beta_i} J_{\alpha,\beta_i} \vec{M}_\alpha \cdot \vec{M}_{\beta_i} \tag{11}$$

Here, α and β are atoms in the crystallographic unit cell and β_i are all the periodic images of the atom β for which a J_{ij} has been calculated.

The use of cMC, in which the magnetizations in Eq. 10 are not quantized, only approximates the correct quantum mechanical result. However, performing Quantum Monte Carlo (QMC)[57] for frustrated systems is generally infeasible because of the negative sign problem.[58] To approximate the correct heat capacity, the value derived from the cMC calculations via the fluctuation-dissipation theorem[59, 60] was transformed according to the scaling proposed by Körmann *et al.*:[21]

$$\frac{C_{V,QMC}(t,S)}{C_{V,cMC}(t,S)} \approx \left(\frac{2t_s/t}{\exp(t_s/t) - \exp(-t_s/t)}\right). \tag{12}$$

Here, t is the normalized temperature $T/T_{C,cMC}$, where the cMC Curie temperature is determined by the peak in the heat capacity $C_{V,cMC}$, and

$$1/t_s \approx 0.54S + 0.54, \tag{13}$$

where S is the localized spin. For a system with more than one atom in its unit cell, the average S is used. Finally, the rescaled heat capacity was numerically integrated to obtain the entropy and free energy. The latter was fitted to a function of the form

$$F_{mag}(T) = A\exp(B/T) + CT^4, \tag{14}$$

where A, B and C are fitting parameters. This ensures interpolation errors smaller than 0.1 meV/atom. F_{mag} is 0 at 0 K because the energy of the ferromagnetic ordering is contained in the DFT calculations.

The most significant contributions to F_{mag} are found around the Curie temperature, where there is a peak in heat capacity. To minimize the error at these conditions, the J_{ij} are therefore recalculated at the volume associated with T_C, obtained from Eq. 3. This was done in an iterative way, until a self-consistent T_C was reached (Fig 2). For numerical stability, the derivative of F_{mag} with respect to volume was not included in the optimization.

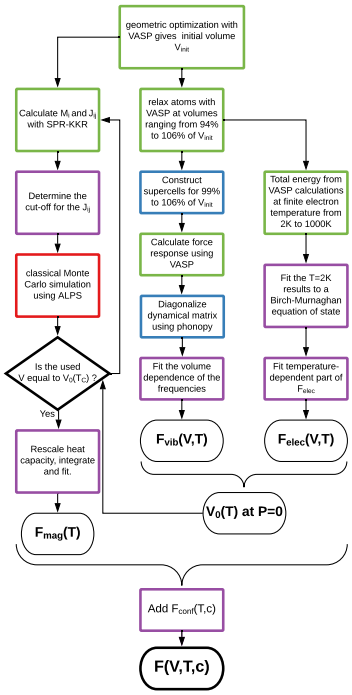

Figure 2: Flowchart indicating the different calculations performed to obtain the free energy. Green indicates a DFT calculation, red an ALPS simulation, blue indicates use of the phonopy software and purple is for standard post-processing.

Magnetic coupling parameters were obtained with spin-polarized scalar-relativistic

DFT calculations in SPR-KKR 6.3 using the PBE functional. The atomic-sphere approximation was applied. The number of E-mesh points was 40 for all calculations with a minimum E-value of -0.2 Ry. The Brillouin zone integration was performed on a $57 \times 57 \times 57$ grid for bulk Fe, a $36 \times 36 \times 36$ grid for Fe_4N and $25 \times 25 \times 25$ grid for $Fe_{16}N_2$. The structure constants R_{max} and G_{max} were set to 2.9 $a.u.$ and 3.3 $a.u.^{-1}$ respectively. The electronic self-consistent field cycle had a convergence criterion of 10^{-5} Ry.

The ALPS classical Monte Carlo calculations were performed with cluster updates for temperatures ranging from 2 K to 1000 K or higher, with the maximum temperature always exceeding T_C by at least 10 % to accurately determine the maximum in the magnetic heat capacity. Periodic boundary conditions were used with a unit cell size of 1000 atoms for Fe, 2560 for Fe_4N and 2250 for $Fe_{16}N_2$. The N atoms were never accounted for in the Heisenberg Hamiltonian, because their magnetic moments, and hence the coupling parameters with neighbors, were negligible. For initial thermalization, 30 000 MC steps were needed. The production phases contained 1 500 000 MC steps for all materials. The input files for all the calculations used in this work can be found in the supplementary information.

The methodology described in this section does not take into account explicit anharmonic contributions or electron-phonon coupling. These were deemed to be of negligible magnitude, because our temperature range of interest lies below half of the melting temperature for the materials that were researched.(grabowski,hickel) The magnon-phonon coupling contributions were not taken into account either. Based on the phonon mode softening for iron at 773 K, their size was estimated to be $1 - 2$ meVatom at the most for our temperature range of interest.

3. Results and Discussion

Because of their limited temperature range of stability and the inability to manufacture isolated specimens, there is very little thermodynamic data available for the Fe_4N and $Fe_{16}N_2$ compounds, especially for the latter. Apart from free energies and heat capacities (Sec. 3.1), we have therefore also calculated structural properties, thermal expansion (Sec.3.2) and bulk moduli (Sec. 3.3), which we have validated with the limited available experimental data where possible. The magnetic contribution to the heat capacity is evaluated separately in Sec. 3.4 and the defect free energy of the N interstitial is discussed in Sec. 3.5. Finally, all the calculated free energies are combined into the phase diagram (Sec. 3.6)

3.1. Free energies and heat capacities

The calculated free energies and heat capacities are shown in Fig. 3 for all three bulk phases at their equilibrium volume at zero pressure. The vibrational, elec-

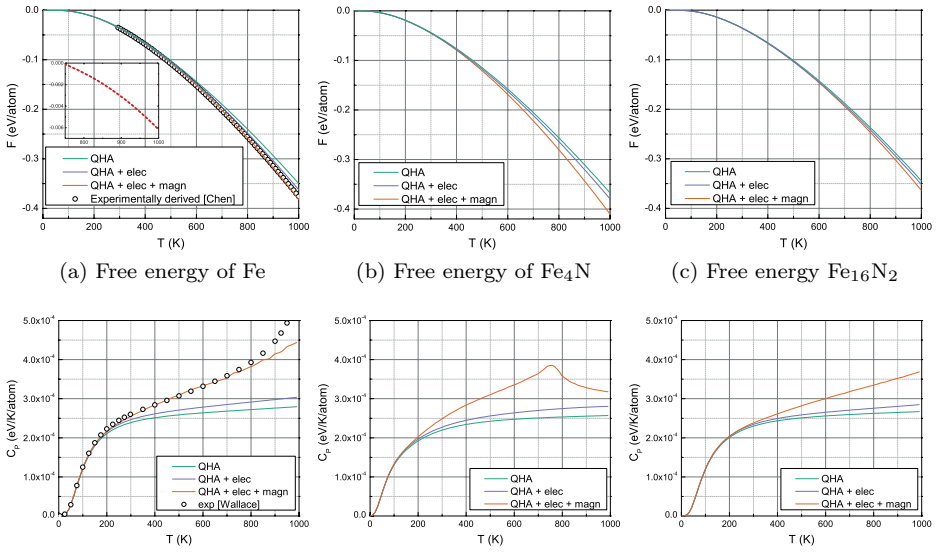

(a) Free energy of Fe (b) Free energy of Fe_4N (c) Free energy $Fe_{16}N_2$

(d) Heat capacity of Fe (e) Heat capacity of Fe_4N (f) Heat capacity of $Fe_{16}N_2$

Figure 3: (Color online) The free energies F [top row, (a)-(c)] and isobaric heat capacities C_P [bottom row, (d)-(f)] of the bulk phases Fe, Fe_4N and $Fe_{16}N_2$ from 0 to 1000 K. The vibrational contributions within the quasiharmonic approximation (QHA), the electronic contributions (elec) and the magnetic contributions (magn) are shown incrementally. For iron, the free energy is compared to the one experimentally derived by Chen *et al.*[62] and the heat capacity is compared to the one recommended by Desai.[63] Inset in a: The difference between the total calculated free energy and the experimentally derived free energy.

tronic and magnetic contributions are plotted separately to indicate their size. The equilibrium volumes at zero pressure are obtained from minimizing the free energy for the entire temperature range of $0 - 1000$ K. This temperature interval was chosen because it is the most relevant for nitiding ferritic steels. [61]

For bulk Fe, ample experimental data are available over its entire range of stability for the isobaric heat capacity C_P. To assess the accuracy of the DFT-derived free energy, it is compared to the data derived from experimental phase equilibria and thermochemical properties.[62] These experimental and our DFT free energies are set equal at room temperature (298 K). The accuracy of the DFT prediction is very good, with a difference of less than 0.1 meV/atom up to 750 K. This confirms the correctness of the methodology, which was previously used to obtain the various contributions to the free energy for Fe and Fe_3C.[21, 22] The excellenct accuracy is also the main argument for utilizing the same approach for Fe_4N and $Fe_{16}N_2$. As can be seen in Fig. 3a, for the free energy of ferrite a somewhat more significant discrepancy starts to occur beyond 850 K, leading to a difference in F of 6 meV/atom between theory and experiment at 1000 K. This is because the quasiharmonic approximation often overestimates anharmonic contributions to the free energy, which typically become important

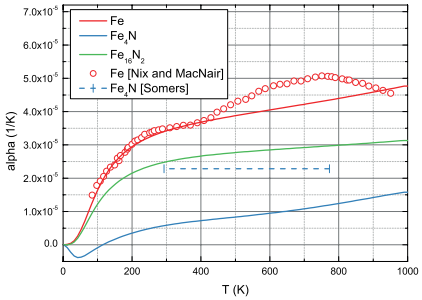

Figure 4: (Color online) DFT-calculated volumetric thermal expansion coefficients of Fe (red), Fe_4N (blue) and $Fe_{16}N_2$ (green). For iron, the experimental data from Nix and MacNair enable a comparison for almost the entire temperature interval.[65]. For Fe_4N, there is only an average expansion coefficient between 293 and 773 K available. At all temperatures, however, the DFT-derived expansion coefficient for Fe_4N constitutes a severe underestimation.

at about half of the melting temperature.[64] For the phase equilibria with Fe_4N and $Fe_{16}N_2$, temperatures above 850 K are not relevant, and the overestimation of the anharmonic contributions poses no problem. In case of the heat capacity of Fe, comparing experimental data[63] with calculated results shows a very good correspondence up to 800 K (Fig. 3d). For higher temperatures, towards the Curie temperature T_C, where the transition between the ferromagnetic and the paramagnetic state occurs, the heat capacity is somewhat underestimated.

For all three phases, the contribution of the electronic entropy to the free energy is the smallest. For Fe, it amounts to a contribution of 4 meV/atom at 750 K, which is nevertheless much larger than the inaccuracy of 0.1 meV/atom at that temperature. This shows the importance of taking all three excitations into account for all materials. For Fe_4N the magnetic contribution to the heat capacity and free energy are larger than for bulk Fe. In contrast, $Fe_{16}N_2$ has a smaller magnetic heat capacity because this material is predicted to have the highest Curie temperature.

3.2. Thermal expansion

The (volumetric) thermal expansion coefficient is defined as

$$\alpha_V = \frac{1}{V}\left(\frac{\partial V}{\partial T}\right)_P . \tag{15}$$

It can be calculated from the derived equilibrium volumes over sufficiently small temperature intervals (10 K), using finite differences. In Fig. 4 this calculated coefficient is shown for Fe, Fe_4N and $Fe_{16}N_2$ as a function of temperature.

The DFT expansion coefficient of bulk Fe compares very well with experimental data, certainly considering the typical error of $0.7\times10^{-5}\,K^{-1}$ for expansion

coefficients derived with QHA.[66] The slight bump in the experimental coefficient that is not accounted for in the DFT result, is considered to stem from the volume dependence of the magnetic heat capacity,[65] which is not taken into account in the calculations. In the case of Fe_4N, an average expansion coefficient was derived experimentally from XRD measurements on powder samples.[14] It is seen that the DFT-obtained expansion severely underestimates that experimental one. The argument made for bulk Fe, that the volume dependence of the magnetic heat capacity is not accounted for in the QHA method as employed in this work, can be made for Fe_4N as well. This might be even more pronounced since it has a lower Curie temperature; $T_C = 750\,\mathrm{K}$ compared to $1044\,K$ for iron.[67] However, the error with respect to the experiment is so large that it cannot be solely explained by such a minor magnetic effect, which are usually secondary to lattice vibrational effects.

If the deviation cannot be attributed to the thermodynamic approach, it must be rooted in the calculated energies and forces. For DFT calculations, the exchange-correlation functional is the main source of deviations from experiment. In this case, the main cause of the large deviation of the PBE functional in predicting the thermal expansion of Fe_4N is most likely the material's unique magneto-volume behavior. A large increase in magnetization occurs close to the equilibrium volume, which PBE is unable to describe well.[68], This volume-dependent magnetic effect can be explained by the covalent nature of the Fe-N bond. As the bond length shortens, the overlap of the $2p$ orbitals of the N atom with the $4s$ orbitals of the nearest-neighbor Fe atoms increases, causing more electron transfer to the N atom.[69] This in turn reduces the screening effect of the $4s$ shell on the $3d$ Fe electrons, causing electron transfer from the $3d$ orbitals of the second nearest-neighbor Fe atoms to those of the Fe atoms nearest to the N atom. Ultimately, compression thus results in a lower magnetic moment on the nearest-neighbor Fe atoms that bond with the N atom.[70] It moreover causes the Fe_4N to be very rigid in the direction of the Fe-N bond, *i.e.* the $< 100 >$ direction.[71]

In an effort to verify that the functional is indeed the source of the discrepancy of the Fe_4N thermal expansion coefficient with respect to experiment, the PBE exchange-correlation functional was swapped for the LDA one. The latter functional differs from PBE in that it positions the LDA equilibrium volume of Fe_4N in the low-magnetization regime rather than at the crossing between low and high magnetization.[68] As can be seen in Fig. 5, the LDA functional does produce a much larger thermal expansion compared to the PBE functional. As expected, the experimental value lies between the LDA and PBE predictions, although the difference between them is much larger than for metals without any covalent character.[72] Possibly, inaccuracies might be present in the experimental measurement because it was taken on a powder sample created from a deposited layer, whereas the calculated expansion is valid for an infinitely large bulk. Regardless, the large impact of the exchange-correlation functional on the calculated expansion coefficient remains a methodological problem. At this

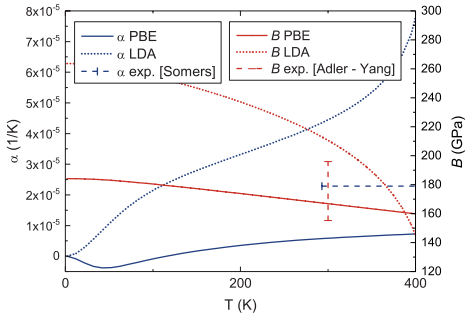

Figure 5: (Color online) A comparison between LDA (dotted lines) and PBE (solid lines) for the calculation of the bulk moduli B (red) and volumetric thermal expansion coefficients α (blue). For the bulk modulus, a large range of experimental values exists (dashed red bar).[73, 74] For the thermal expansion, the value determined by Somers *et al.* is an average for the temperature range 293 to 773 K.[14]

point, it is not clear whether there is another functional or another (feasible) level of theory that can provide a better description of both the covalent nature of the Fe-N bond, the unique magnetic behavior of Fe_4N and the $Fe_{16}N_2$ and bulk Fe phases.

3.3. Bulk modulus

The temperature-dependent bulk modulus, or inverse of the compressibility,

$$B(T) = V_0 \left(\frac{\partial^2 F}{\partial V^2} \right)_T \Bigg|_{V=V_0} \tag{16}$$

can be directly obtained from the above results and the derivatives of the analytic expressions for the various contributions to the free energy (Eqs. 5-9). In Fig 6 the bulk modulus is shown for all three phases. As far as Fe is concerned, the calculated bulk modulus at 0 K is too high by about 15 GPa compared to experimental data. This is in contrast to the typical trend for PBE, which usually underestimates bulk moduli by about 5%.[75] On the other hand, it is typical for magnetic materials to buck this trend, as a generalized-gradient approximation (GGA) such as PBE tends to overestimate the magnetic energy.[76] The slope of the Fe bulk modulus is reproduced quite well, with the experimental one being overall slightly less steep compared to the DFT result. Much fewer data are available on bulk moduli for Fe_4N and $Fe_{16}N_2$, because these phases usually only exist as precipitates or as a deposited layer. In fact, there are no experimental data for $Fe_{16}N_2$ whatsoever and the experimentally determined bulk moduli that are available for Fe_4N have a large spread (Fig. 6). A possible reason for these large experimental deviations, is the difference in measurement methodology. It varies from nanoindentation to high-pressure X-ray diffraction (XRD) measurements, both on powdered samples and on bulk-like

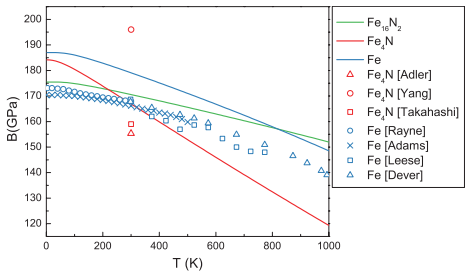

Figure 6: DFT-calculated (line) and experimental (symbol) bulk moduli B for Fe, Fe_4N and $Fe_{16}N_2$. For Fe, a combination of data from different authors is made to cover the temperature range from 0 to 1000 K.[78, 79, 80, 81] A wide range of experimental data are available for Fe_4N, all at room temperature (red symbols).[73, 74, 77]

samples.[74, 73, 77] The combination with the difficulty of obtaining pure samples makes it very cumbersome to compare different experimental procedures. The calculated Fe_4N bulk modulus falls in the range of the experimental values. The strong dependence on temperature moreover confirms the volume-sensitive behavior of Fe_4N compared to the other two materials. Just as was the case for the thermal expansion (Sec. 3.2), this volume-sensitive behavior causes a large discrepancy between the LDA and PBE functionals (Fig. 5).

3.4. Magnetic properties of the bulk phases

The magnetic contribution to the free energy is significant, even at temperatures well below the Curie temperature (Fig. 3), and thus requires a high degree of accuracy. It was found that this high accuracy can be reached through the rescaling procedure of Körmann *et al.*, provided the Curie temperature is predicted accurately.[21] For this reason, effective nearest-neighbor magnetic exchange coefficients J_{ij} are sometimes fit to the experimental Curie temperature to obtain the magnetic heat capacity.[22, 18] This work, however, aims to use a methodology also able to predict the Curie temperature. Therefore, the J_{ij} were determined from first principles and the Curie temperature was identified as the temperature at which the resulting heat capacity reaches its peak.[82] The quality of the predicted Curie temperature is then a measure for the accuracy of the magnetic free energy.

For Fe and Fe_4N, the DFT-derived Curie temperature (Fig 7) corresponds very well with the experimental one. It is also evident that the disappearance of the magnetization is a poor measure to determine the transition to the paramagnetic state; this is an experimental issue as well.[83] The finite size of the simulation cells is responsible for some remanant magnetization above the critical temperature. For $Fe_{16}N_2$ the experimental Curie temperature is much lower than the one derived from the simulations. The experimental magnetization goes to zero when 800 K is reached, but with the exchange coefficients and magnetization derived from DFT, a critical temperature of about 1300 K is found. In an extensive

evaluation of different methods to obtain the Curie temperature for $Fe_{16}N_2$, Ke *et al.* concluded that the experimental value is most likely significantly too low. [84] Instead, it is proposed that $Fe_{16}N_2$ has a higher Curie temperature than the one experimentally derived and also higher than the one found for Fe. For this reason, unfilled symbols are used to show the experimental results for the magnetization of $Fe_{16}N_2$ in Fig. 7.

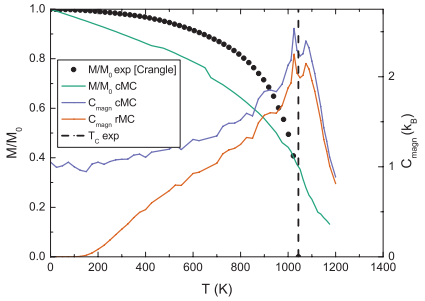

(a) Fe

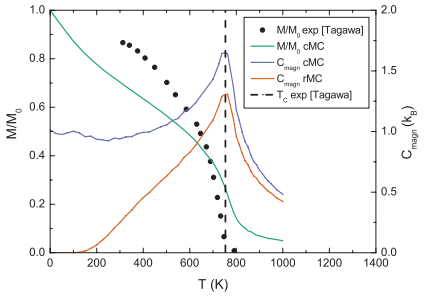

(b) Fe_4N

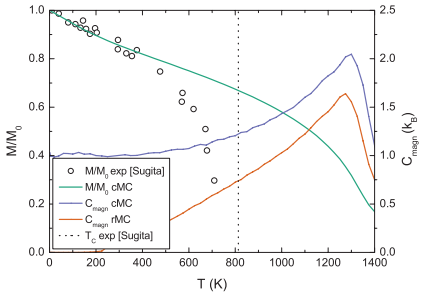

(c) $Fe_{16}N_2$

Figure 7: (Color online) Calculated magnetization (M/M_0) and magnetic contribution C_{magn} to the heat capacity for Fe, Fe_4N and $Fe_{16}N_2$. Experimentally measured magnetizations and subsequently derived Curie temperatures are included for all three phases (black).[85, 67, 86] The experimental data for the magnetization of $Fe_{16}N_2$ are shown in unfilled circles to emphasize their problematic nature (see text). To compare the experimental magnetizations with those derived from the classical Monte Carlo (cMC) simulations, both are normalized to their respective magnetizations at 0 K. For the heat capacity, both the direct result from the cMC simulations (blue) and the rescaled result (rMC),(red) are presented, the latter serving as approximation for the quantum Monte Carlo result.

3.5. Interstitial nitrogen defect

The defect free energy of interstitial nitrogen is obtained using the supercell method. In this approach, the crystallographic unit cell of the bulk material is multiplied and a defect is inserted. In the case of the nitrogen interstitial, a N atom is inserted in the bulk Fe supercell on an octahedral position (see Fig. 1c). The local distortion caused by the defect is captured by optimizing all atomic positions. It is debatable whether the volume and shape of the defect supercell should be optimized as well. On the one hand, maintaining the bulk geometry helps to isolate the defect from its periodic images, as it cuts out long-range elastic interactions. However, this imposes a stress on the supercell which depends on the N concentration. On the other hand, if one wishes to remove those stresses by allowing full optimization of the shape and size of the unit cell, a larger computational investment might be necessary. Both approaches were evaluated for different supercell sizes. The energy of solution U_{sol} is obtained by subtracting the DFT-obtained total energy of the defect-free supercell and the isolated N_2 molecule from the total energy of the supercell with the defect. In Fig. 8 the dependence of U_{sol} on the used supercell size is shown. It shows that the constant-pressure (stress-free) and constant-volume approach converge towards a common limit, ultimately yielding the same defect energy as supercell size is increased. Using a 250-atom supercell for either method a precision of the calculation of about 10 meV/defect can be achieved for U_{sol}. The 250-atom $U_{sol} = 0.133\ eV$ of the constant-volume approach was used in the remainder of this work, because that approach converges somewhat more rapidly.

Insight in the phase equilibrium between Fe_4N, $Fe_{16}N_2$ and $Fe_{[N]}$ (sec. 3.6) requires accounting for the entropy of the defect as well. In Fig. 9 the configurational contribution is shown to be largest, but both the vibrational and the electronic free energy have to be taken into account as well. The electronic part can be obtained in a similar way as for bulk materials. For the vibrational contribution, full phonon spectra are calculated for the supercells containing the defect and QHA is used. Because the presence of the N atom in the Fe matrix breaks most of the symmetry, a large number of force calculations is then necessary to obtain the phonon spectra. Alternatively, the less expensive partial Hessian method can be used, which only requires the frequencies of the N atom in a fixed Fe matrix. The three frequencies obtained can be used to apply a simplified form of Eq. 9. From Fig. 9 it can be seen the differences between feasible supercell sizes are still quite large. An uncertainty of 0.2 eV/defect remains for a 54-atom cell, which is as large as for the partial Hessian method that is also not sufficiently precise. This large uncertainty is not surprising; it is the same order of magnitude as for U_{sol} (see Fig. 8). Ultimately, by using a highly converged U_{sol} 250-atom and the vibrational and electronic entropies from a 128-atom supercell, one expects a remaining uncertainty of 10 meV/atom for the vibrational contribution. Combined with the uncertainty for 10K (U_{sol}), this results in a total uncertainty of $20 to 30$ meV/atom.

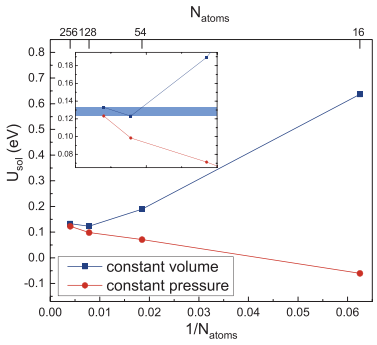

Figure 8: (Color online) Convergence of the N interstitial defect energy at 0 K as a function of inverse supercell size. The absolute value of the defect energy is with reference to the N_2 gaseous state: $Fe_{solid} + \frac{1}{2}N_2 \rightarrow Fe_{[N],solid}$. Inset: The convergence for the larger supercells in more detail. A residual uncertainty of 10 meV/defect remains (blue rectangle).

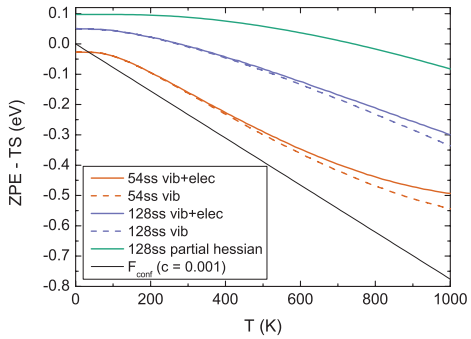

Figure 9: (Color online) A comparison of the different methods to obtain the finite-temperature energetic contributions for N in solid solution in Fe. The configurational part, shown here for a typical concentration of 0.1 at.% is always the largest, but both the electronic and vibrational free energies cannot be neglected. In comparison with the 128-atom supercell, the simple partial Hessian approach (see text) yields frequencies that are overestimated, whereas a 54-atom supercell underestimates the frequencies.

3.6. Phase equilibria

With the free energies of Fe, Fe_4N, $Fe_{16}N_2$ and $Fe_{[N]}$, all information is available to predict their phase equilibria, resolving the experimental uncertainties that have hindered insight and further development of the Fe-N system. The question of the (meta)stability of $Fe_{16}N_2$, for example, is still a contemporary topic.[87] The driving force ΔF for the formation of $Fe_{16}N_2$ from Fe_4N and $Fe_{[N]}$ is

$$\Delta F(T) = F_{\mathrm{Fe_{16}N_2}}(T) - \frac{2 - 18c_{lim}}{1 - 5c_{lim}} F_{\mathrm{Fe_4N}}(T) - \frac{8}{1 - 5c_{lim}} F_{\mathrm{Fe}}(T), \qquad (17)$$

if one supposes the transformation takes place in the bulk of a large environment of Fe with interstitial N present in equilibrium concentration c_{lim} (see further). The free energy difference can be obtained from the calculated free energies at equilibrium volumes V_0 in this work and is presented in Fig. 10. We find that $Fe_{16}N_2$ is stable at low temperatures ($\Delta F < 0$) and decomposition becomes energetically favorable above 400 K ($\Delta F > 0$). This is consistent with the experimental finding that decomposition starts between 470 K and 520 K. The experimentally higher decomposition temperature is explained by the required activation energy for N diffusion.[88, 84] In experiment too, there is an indication that $Fe_{16}N_2$ becomes thermodynamically unstable between $400-450$ K, *i.e.* before decomposition occurs. The temperature-dependent change in c/a-ratio, measured very precisely by Widenmeyer *et al.*,[88] shows a sharp rise starting from $400 - 450$ K (Fig. 10). Widenmeyer *et al.* proposed that this stems from a loss of order of the N atoms on the interstitial sublattice of $Fe_{16}N_2$, thus suggesting a transition to a disordered Fe_8N phase. It is possible to obtain a temperature-dependent $c/a-$ratio from our DFT results via the calculated volume-dependent $c/a-$ratio and the temperature-dependent equilibrium volume derived with QHA. As shown in Fig. 10, the QHA $c/a-$ratio is practically invariant with temperature, which strengthens the argument that the experimentally observed variation is caused by loss of N ordering, as the N-atoms were kept ordered on their sublattice in the calculations. It also sheds a new light on the experimentally derived Curie temperature for $Fe_{16}N_2$.[89] The measured drop in magnetization becomes more pronounced from 400 K onward (Fig. 7), the point where $Fe_{16}N_2$ becomes thermally unstable according to the DFT result. Consequently, the magnetizations measured above 400 K, and the derived Curie temperature, should be associated with the disordered Fe_8N structure.

To complete the phase diagram for $Fe_{[N]}$, Fe_4N and $Fe_{16}N_2$, the concentration limit of solubility $c_{lim}(T)$ can be derived from the defect free energy of the N interstitial F_{def}, the free energy of Fe, the free energy of Fe_4N and the free energy of $Fe_{16}N_2$:

$$4F_{\mathrm{Fe}}(T) + F_{def}(T, c_{lim}(T)) = F_{\mathrm{Fe_4N}}(T). \qquad (18)$$

$$16F_{\mathrm{Fe}}(T) + 2F_{def}(T, c_{lim}(T)) = F_{\mathrm{Fe_{16}N_2}}(T). \qquad (19)$$

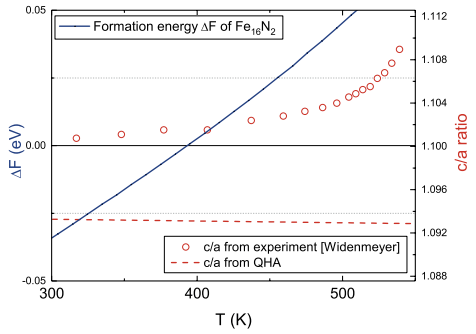

Figure 10: (Color online) Left axis (blue): from the DFT calculations, it can be concluded that $Fe_{16}N_2$ becomes thermodynamically unstable with respect to dissociation into Fe_4N and bulk Fe (solid line) above 400 K. Right axis (red): a comparison of the experimental c/a ratio of $Fe_{16}N_2$ (circles)[88] with the one derived via the quasiharmonic approximation (dashed line). The sharp increase starting at 400-450 K measured in experiment is not observed computationally (see text for interpretation).

The final phase diagram, with all three phase equilibria, is presented in Fig. 11. The computationally derived solubility limit of N in bulk Fe is compared to the experimental data assembled by Wriedt *et al.*[27]. In the case of the solvus, good correspondence with experimental data is achieved by using the defect free energy from the 128-atom supercell. The large discrepancy with the 54-atom thus shows the importance of using this larger supercell. For the phase boundary between $Fe_{16}N_2$ and its dissociation in Fe_4N and bulk Fe, no experimental data are available, but the accuracy is expected to be very high. As discussed in Sec. 3.1, the free energy for Fe is very accurate below half of its melting temperature. Because of the similarity of Fe_4N and $Fe_{16}N_2$ and the correct calculation of the Curie temperatures, the same is expected for these bulk phases.

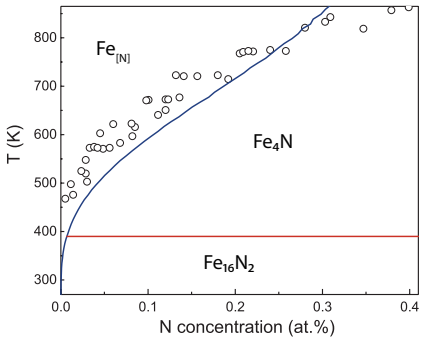

Figure 11: (Color online) The DFT-obtained phase diagram of $Fe_{[N]}$, Fe_4N and $Fe_{16}N_2$. Experimental data for the limit of solubility of N in Fe are included for comparison (circles).[27]

4. Conclusion

Despite the industrial importance of nitriding for the post-treatment of steel, there is still a lack of understanding with respect to the properties of the governing Fe-N phases. In this work, we established the thermodynamic behavior of $Fe_{16}N_2$, Fe_4N and Fe with N in solid solution and used it to elucidate the Fe-N phase diagram in the low-nitrogen limit (see Fig. 10). Phase equilibria were determined using density-functional theory, which avoids the need for any experimental input. This is particularly useful for Fe_4N and $Fe_{16}N$, for which large homogeneous samples are not experimentally available. Vibrational contributions to the free energy were derived with the quasiharmonic approximation, while the magnetic free energy was calculated using Monte Carlo simulations based on a Heisenberg model. Several potential sources of numerical errors were identified in the process, leading in most cases to limited errors. The largest error bar originates from the supercell size used to model the free energy of interstitial nitrogen; this error is about $14 - 20$ meV/defect at 0 K using a 128-atom supercell.

Using our calculations, we were able to determine the free energy, heat capacity, thermal expansion and bulk modulus of Fe, Fe_4N and $Fe_{16}N_2$ as a function of temperature. While experimental data are available for Fe which allowed us to check the validity of our first-principles approach, these quantities are mostly not available for the Fe_4N and $Fe_{16}N_2$ phases, as these materials are experimentally hard to manufacture in bulk. Only for the thermal expansion coefficient of Fe_4N, a strong underestimation of the experimental result was found. A comparison of the LDA and PBE exchange-correlation functional revealed that the unique coupling between magnetism and crystal volume exacerbates the impact of functional inadequacies. A better description of the volume dependence of Fe_4N therefore requires the development of improved exchange-correlation functionals, which are able to capture both the covalent and magnetic characteristics correctly. This is in linen with the conclusion from Blancá *et al.*[68] Furthermore, both the calculation of phonon-magnon coupling contributions for Fe_4N and $Fe_{16}N_2$ and explicit anharmonicity for the nitrogen defect could be valuable additions to the calculated free energies.

Based on DFT-calculated free energies, the phase diagram of $Fe_{[N]}$,Fe_4N and $Fe_{16}N_2$ was constructed, yielding an accurate representation of the nitrogen solvus and providing a closer view on the stability of $Fe_{16}N_2$. We find $Fe_{16}N_2$ to be thermodynamically stable at low temperatures and to decompose into Fe_4N and Fe around 400 K. Experimental dissociation happens above 470 K, with the difference attributed to the required activation energy for nitrogen mobility. In addition, we note that the experimentally established Curie temperature for $Fe_{16}N_2$ cannot be attributed to the pure $Fe_{16}N_2$ phase, but is affected by the experimentally observed loss of nitrogen order between 400 and 450 K. This is also supported by a comparison between experimental measurements of the c/a-ratio as a function of temperature and our quasiharmonic DFT results.

Our results fill in a long-standing gap in the knowledge on the Fe-N system. The predicted free energies, heat capacities, equilibrium volumes and bulk moduli can now be used in larger-scale approaches, such as phase field models.[8] These approaches can aid in describing precipitation and transformation in the Fe-N system from a more macroscopic point of view. This is essential to increase the applicability of nitriding and lays the foundations to understand ternary nitrogen-containing compounds.

Acknowledgments

Sam De Waele and Stefaan Cottenier acknowledge financial support from OCAS NV by an OCAS–endowed PhD position and by an OCAS–endowed chair at Ghent University, respectively. This work moreover benefited from the Research Foundation Flanders (FWO) through the personal postdoctoral fellowship of Kurt Lejaeghere and [project Nr. G0E0116N]. The computational resources and services used in this work were provided by the VSC (Flemish Supercomputer Center), funded by the Research Foundation Flanders (FWO) and the Flemish Government – department EWI.

[1] G. Miyamoto, Y. Tomio, H. Aota, K. Oh-ishi, K. Hono, and T. Furuhara, Materials Science and Technology **27**, 742 (2011).

[2] M. Somers (Chennai, India, 2013).

[3] O. Singh, H. K. Malik, R. P. Dahiya, and P. K. Kulriya, Journal of Alloys and Compounds **710**, 253 (2017).

[4] W. Dal'Maz Silva, J. Dulcy, J. Ghanbaja, A. Redjaïmia, G. Michel, S. Thibault, and T. Belmonte, Materials Science and Engineering: A **693**, 225 (2017).

[5] X. C. Xiong, *Élaboration et genèse des microstructures dans les "aciers" fer-azote* (Vandoeuvre-les-Nancy, INPL, 2008).

[6] L. C. Gontijo, R. Machado, E. J. Miola, L. C. Casteletti, and P. A. P. Nascente, Surface and Coatings Technology **183**, 10 (2004).

[7] H. Göhring, A. Leineweber, and E. J. Mittemeijer, Metallurgical and Materials Transactions A **46**, 3612 (2015).

[8] H. Liu, Y. Gao, J. Z. Liu, Y. M. Zhu, Y. Wang, and J. F. Nie, Acta Materialia **61**, 453 (2013).

[9] H. Göhring, O. Fabrichnaya, A. Leineweber, and E. J. Mittemeijer, Metallurgical and Materials Transactions A **47**, 6173 (2016).

[10] S. Shang and A. J. Böttger, Acta Materialia **53**, 255 (2005).

[11] P. Hohenberg and W. Kohn, Physical Review **136**, B864 (1964).

[12] W. Kohn and L. Sham, Physical Review **140**, 1133 (1965).

[13] H. Grabke, Berichte der Bunsengesellschaft für physikalische Chemie **73**, 596 (1969).

[14] M. a. J. Somers, N. M. v. d. Pers, D. Schalkoord, and E. J. Mittemeijer, Metallurgical Transactions A **20**, 1533 (1989).

[15] B. J. Kooi, M. A. J. Somers, and E. J. Mittemeijer, Metallurgical and Materials Transactions A **27**, 1063 (1996).

[16] M. I. Pekelharing, A. J. Böttger, and E. J. Mittemeijer, Philosophical Magazine **83**, 1775 (2003).

[17] M. I. Pekelharing and A. J. Böttger, Computational Materials Science **45**, 561 (2009).

[18] F. Körmann, Y. Ikeda, B. Grabowski, and M. H. F. Sluiter, npj Computational Materials **3**, 36 (2017).

[19] G. Bonny, N. Castin, C. Domain, P. Olsson, B. Verreyken, M. I. Pascuet, and D. Terentyev, Philosophical Magazine **0**, 1 (2016).

[20] N. D. Mermin, Physical Review **137**, A1441 (1965).

[21] F. Körmann, A. Dick, T. Hickel, and J. Neugebauer, Physical Review B **81**, 134425 (2010).

[22] A. Dick, F. Körmann, T. Hickel, and J. Neugebauer, Physical Review B **84**, 125101 (2011).

[23] K. H. Jack, Journal of Alloys and Compounds **222**, 160 (1995).

[24] K. H. Jack, Acta Crystallographica **3**, 392 (1950).

[25] C. Domain, C. S. Becquart, and J. Foct, Physical Review B **69**, 144112 (2004).

[26] D. C. Wallace, *Thermodynamics of Crystals* (Courier Corporation, 1998).

[27] H. A. Wriedt, N. A. Gokcen, and R. H. Nafziger, Bulletin of Alloy Phase Diagrams **8**, 355 (1987).

[28] H. V. Keer, *Principles of the Solid State* (New Age International, 1993).

[29] B. Grabowski, P. Söderlind, T. Hickel, and J. Neugebauer, Physical Review B **84**, 214107 (2011).

[30] F. Birch, Physical Review **71**, 809 (1947).

[31] G. Kresse and J. Furthmüller, Computational Materials Science **6**, 15 (1996).

[32] G. Kresse and J. Furthmüller, Physical Review B **54**, 11169 (1996).

[33] G. Kresse and D. Joubert, Physical Review B **59**, 1758 (1999).

[34] G. Kresse, M. Marsman, and J. Furthmüller, "VASP the GUIDE," (2015).

[35] K. Lejaeghere, G. Bihlmayer, T. Björkman, P. Blaha, S. Blügel, V. Blum, D. Caliste, I. E. Castelli, S. J. Clark, A. D. Corso, S. d. Gironcoli, T. Deutsch, J. K. Dewhurst, I. D. Marco, C. Draxl, M. Dułak, O. Eriksson, J. A. Flores-Livas, K. F. Garrity, L. Genovese, P. Giannozzi, M. Giantomassi, S. Goedecker, X. Gonze, O. Grånäs, E. K. U. Gross, A. Gulans, F. Gygi, D. R. Hamann, P. J. Hasnip, N. a. W. Holzwarth, D. Iuşan, D. B. Jochym, F. Jollet, D. Jones, G. Kresse, K. Koepernik, E. Küçükbenli, Y. O. Kvashnin, I. L. M. Locht, S. Lubeck, M. Marsman, N. Marzari, U. Nitzsche, L. Nordström, T. Ozaki, L. Paulatto, C. J. Pickard, W. Poelmans, M. I. J. Probert, K. Refson, M. Richter, G.-M. Rignanese, S. Saha, M. Scheffler, M. Schlipf, K. Schwarz, S. Sharma, F. Tavazza, P. Thunström, A. Tkatchenko, M. Torrent, D. Vanderbilt, M. J. v. Setten, V. V. Speybroeck, J. M. Wills, J. R. Yates, G.-X. Zhang, and S. Cottenier, Science **351**, aad3000 (2016).

[36] J. P. Perdew, K. Burke, and M. Ernzerhof, Physical Review Letters **77**, 3865 (1996).

[37] J. P. Perdew and A. Zunger, Physical Review B **23**, 5048 (1981).

[38] K. Kunc and R. M. Martin, Physical Review Letters **48**, 406 (1982).

[39] A. Togo and I. Tanaka, Scripta Materialia **108**, 1 (2015).

[40] M. Methfessel and A. T. Paxton, Physical Review B **40**, 3616 (1989).

[41] N. M. Rosengaard and B. Johansson, Physical Review B **55**, 14975 (1997).

[42] M. Pajda, J. Kudrnovský, I. Turek, V. Drchal, and P. Bruno, Physical Review B **64**, 174402 (2001).

[43] M. Ležaić, P. Mavropoulos, and S. Blügel, Applied Physics Letters **90**, 082504 (2007).

[44] A. V. Ruban, S. Khmelevskyi, P. Mohn, and B. Johansson, Physical Review B **75**, 054402 (2007).

[45] G. Y. Gao, K. L. Yao, E. Şaşıoğlu, L. M. Sandratskii, Z. L. Liu, and J. L. Jiang, Physical Review B **75**, 174442 (2007).

[46] F. Körmann, A. Dick, B. Grabowski, B. Hallstedt, T. Hickel, and J. Neugebauer, Physical Review B **78**, 033102 (2008).

[47] F. Körmann, A. Dick, T. Hickel, and J. Neugebauer, Physical Review B **83**, 165114 (2011).

[48] J. Korringa, Physica **13**, 392 (1947).

[49] W. Kohn and N. Rostoker, Physical Review **94**, 1111 (1954).

[50] H. Ebert et al., "The Munich SPR-KKR package," .

[51] H. Ebert, D. Ködderitzsch, and J. Minár, Reports on Progress in Physics **74**, 096501 (2011).

[52] A. I. Liechtenstein, M. I. Katsnelson, and V. A. Gubanov, Journal of Physics F: Metal Physics **14**, L125 (1984).

[53] N. Metropolis, A. W. Rosenbluth, M. N. Rosenbluth, A. H. Teller, and E. Teller, The Journal of Chemical Physics **21**, 1087 (1953).

[54] A. F. Albuquerque, F. Alet, P. Corboz, P. Dayal, A. Feiguin, S. Fuchs, L. Gamper, E. Gull, S. Gürtler, A. Honecker, R. Igarashi, M. Körner, A. Kozhevnikov, A. Läuchli, S. R. Manmana, M. Matsumoto, I. P. McCulloch, F. Michel, R. M. Noack, G. Pawłowski, L. Pollet, T. Pruschke, U. Schollwöck, S. Todo, S. Trebst, M. Troyer, P. Werner, and S. Wessel, Journal of Magnetism and Magnetic Materials **310**, 1187 (2007).

[55] B. Bauer, L. D. Carr, H. G. Evertz, A. Feiguin, J. Freire, S. Fuchs, L. Gamper, J. Gukelberger, E. Gull, S. Guertler, A Hehn, R. Igarashi, S. V. Isakov, D. Koop, P. N. Ma, P. Mates, H. Matsuo, O. Parcollet, G. Pawłowski, J. D. Picon, L Pollet, E. Santos, V. W. Scarola, U. Schollwöck, C. Silva, B. Surer, S. Todo, S. Trebst, M. Troyer, M. L. Wall, P Werner, and S. Wessel, Journal of Statistical Mechanics: Theory and Experiment **2011**, P05001 (2011).

[56] P. W. Anderson, Solid State Physics **14**, 99 (1963).

[57] A. W. Sandvik and J. Kurkijärvi, Physical Review B **43**, 5950 (1991).

[58] P. Henelius and A. W. Sandvik, Physical Review B **62**, 1102 (2000).

[59] H. Nyquist, Physical Review **32**, 110 (1928).

[60] H. B. Callen and T. A. Welton, Physical Review **83**, 34 (1951).

[61] Mittemeijer, "Fundamentals of Nitriding and Nitrocarburizing - Heat Treating Society," .

[62] Q. Chen and Z. Jin, Metallurgical and Materials Transactions A **26**, 417 (1995).

[63] P. D. Desai, Journal of Physical and Chemical Reference Data **15**, 967 (1986).

[64] A. Glensk, B. Grabowski, T. Hickel, and J. Neugebauer, Physical Review Letters **114**, 195901 (2015).

[65] F. C. Nix and D. MacNair, Physical Review **60**, 597 (1941).

[66] K. Lejaeghere, J. Jaeken, V. Van Speybroeck, and S. Cottenier, Physical Review B **89**, 014304 (2014).

[67] K. Tagawa, E. Kita, and A. Tasaki, Japanese Journal of Applied Physics **21**, 1596 (1982).

[68] E. L. P. y. Blancá, J. Desimoni, N. E. Christensen, H. Emmerich, and S. Cottenier, Physica Status Solidi (B) **246**, 909 (2009).

[69] W. Zhou, L.-j. Qu, Q.-m. Zhang, and D.-s. Wang, Physical Review B **40**, 6393 (1989).

[70] D. Li, J. W. Roh, K. J. Jeon, Y. S. Gu, and W. Lee, Physica Status Solidi (B) **245**, 2581 (2008).

[71] T. Gressmann, M. Wohlschlögel, S. Shang, U. Welzel, A. Leineweber, E. J. Mittemeijer, and Z. K. Liu, Acta Materialia **55**, 5833 (2007).

[72] B. Grabowski, T. Hickel, and J. Neugebauer, Physical Review B **76**, 024309 (2007).

[73] J. F. Adler and Q. Williams, Journal of Geophysical Research: Solid Earth **110**, B01203 (2005).

[74] C. L. Yang, M. M. Abd-Elmeguid, H. Micklitz, G. Michels, J. W. Otto, Y. Kong, D. S. Xue, and F. S. Li, Journal of Magnetism and Magnetic Materials **151**, L19 (1995).

[75] K. Lejaeghere, V. Van Speybroeck, G. Van Oost, and S. Cottenier, Critical Reviews in Solid State and Materials Sciences **39**, 1 (2013).

[76] D. J. Singh and J. Ashkenazi, Physical Review B **46**, 11570 (1992).

[77] T. Takahashi, J. Burghaus, D. Music, R. Dronskowski, and J. M. Schneider, Acta Materialia **60**, 2054 (2012).

[78] J. A. Rayne and B. S. Chandrasekhar, Physical Review **122**, 1714 (1961).

[79] J. J. Adams, D. S. Agosta, R. G. Leisure, and H. Ledbetter, Journal of Applied Physics **100**, 113530 (2006).

[80] J. Leese and A. E. Lord, Journal of Applied Physics **39**, 3986 (1968).

[81] D. Dever, Journal of Applied Physics **43**, 3293 (1972).

[82] J. Weber, Physical Review **101**, 1620 (1956).

[83] R. G. Harrison, Journal of Applied Physics **115**, 033901 (2014).

[84] L. Ke, K. D. Belashchenko, M. van Schilfgaarde, T. Kotani, and V. P. Antropov, Physical Review B **88**, 024404 (2013).

[85] J. Crangle and G. M. Goodman, Proceedings of the Royal Society of London A **321**, 477 (1971).

[86] Y. Sugita, H. Takahashi, M. Komuro, K. Mitsuoka, and A. Sakuma, Journal of Applied Physics **76**, 6637 (1994).

[87] S. Yamamoto, R. Gallage, Y. Ogata, Y. Kusano, N. Kobayashi, T. Ogawa, N. Hayashi, K. Kohara, M. Takahashi, and M. Takano, Chemical Communications **49**, 7708 (2013).

[88] M. Widenmeyer, T. C. Hansen, and R. Niewa, Zeitschrift für anorganische und allgemeine Chemie **639**, 2851 (2013).

[89] Y. Sugita, Journal of Applied Physics **70**, 5977 (1991).